MECHANICS OF A HYPERELASTIC INFLATED TUBE WITH EMPHASIS ON BIOLOGICAL SOFT TISSUES

Ömer Faruk BÜYÜKKAYA *[ID]
Ali Fethi OKYAR *[ID]

Abstract: Inflated hollow cylinder is an important problem encountered in a variety of fields in engineering. In industry, tires and fire hoses are pressurized from inside. In biomechanics, veins, arteries and intervertebral discs can also be modeled using the inflated cylinder problem. The soft ground substance of biological tissues in question are incompressible and portray large non-linear deformations under loading. Classical theories of linear elasticity are incapable of modeling such behavior. Instead, continuum mechanics based large displacement formulation and hyperelasticity are necessary to understand the deformation and mechanics of soft materials. In this study, inflation of a cylinder composed of an isotropic neo-Hookean type of material is analyzed in plane strain and generalized plane strain conditions. First, an analytical solution is established using a continuum mechanical framework. Second, the finite element method is employed to model the same problem. The numerical approach is verified by using a mesh sensitivity analysis and validated by using analytical solution. Therefore, the proposed analytical benchmark can quantify the accuracy of any commercial finite element software solution of neo-Hookean tube inflation. As a side result, it was also revealed that the hydrostatic pressure in the tube is more than six times the inflation pressure.

Keywords: Hyperelasticity, Continuum Mechanics, Finite Element Method, Annular Cylinder, Biological Tissue

Biyolojik Dokulara Vurgu ile Şişirilmiş Hiperelastik bir Tüpün Mekaniği

Öz: İçi boş bir silindirin şişirilmesi, mühendisliğin çeşitli alanlarında karşılaşılan önemli bir problemdir. Endüstride, araba lastikleri ve itfaiye hortumları içten basınçlandırılırlar. Biyomekanikte, damarlar ve intervertebral diskler de şişirilmiş silindir problemi kullanılarak modellenebilir. Bahsedilen biyolojik dokuların yumuşak yapısı sıkıştırılamazlar ve yük altında büyük, doğrusal olmayan deformasyon sergilerler. Klasik doğrusal elastik teoriler böyle bir davranışı modellemede yetersiz kalır. Bunun yerine, yumuşak malzemelerin deformasyonu ve mekaniğini anlamak için sürekli ortamlar mekaniği temelli yüksek yer değiştirme formülasyonları gereklidir. Bu çalışmada, izotropik neo-Hookean malzemeden meydana gelen hiperelastik bir tüp düzlemsel gerinim ve genelleştirilmiş düzlemsel gerinim koşulları altında analiz edilmiştir. İlk olarak, her iki koşul için sürekli ortamlar mekaniği çerçevesinde bir analitik çözüm inşa edilmiştir. Sonrasında, aynı problem için sonlu elemanlar yöntemi işleme konulmuştur. Nümerik modelin doğrulaması ağ hassasiyet analizi kullanılarak sağlanmıştır. Analitik çözüm ile doğrulanmıştır. Buradan, öne sürülen analitik çözüm ile herhangi bir ticari sonlu elemanlar yazılımı ile elde edilmiş şişirilen neo-Hookean bir tüpün davranış hassasiyeti belirlenebilecektir. Analitik çözümle gelen ilginç bir yan sonuç, tüpün içerisindeki hidrostatik basıncın şişirme basıncından altı kat fazla çıkması olmuştur.

Anahtar Kelimeler: Hiperelastisite, Sürekli Ortamlar Mekaniği, Sonlu Elemanlar Yöntemi, Anüler Silindir, Biyolojik Doku

---

* Yeditepe Üniversitesi, Mühendislik Fakültesi, Ataşehir 34755 İstanbul
  Correspondence Author: Ömer Faruk Büyükkaya (omerfaruk.buyukkaya@std.yeditepe.edu.tr)

1. INTRODUCTION

Pressurized cylinders are quite commonly studied in engineering. For example, the problems encountered in pressure vessels and automobile tires can both be viewed as such. In the human body, veins, and annulus fibrosus are also modeled as pressurized cylinders. Although the simplifying elasticity assumption of thin-walled cylinders (Goodno & Gere, 2016) is adequate to model a metallic pressurized vessel structure, this is not so for the case of a tire or vein, due to their underlying nonlinear material behavior and wall thickness. Rubber-like materials that exhibit exceptionally large, non-linear deformations under small loads when compared to conventional metals and ceramics are called hyperelastic materials. Rubbers and biological soft tissues behave in a nearly incompressible manner. This is embedded into the hyperelastic material model as an additional internal constraint: unchangeability (incompressibility) of the volume. In order to analyze such complex mechanical behavior, continuum mechanics methodology has been employed.

In hyperelasticity, strain energy density plays a central role in providing the characteristic mechanical behavior. Several general formulae have been proposed for the strain energy density function, portraying characteristics of different material types through the years. The most well-known theories are neo-Hookean (Treloar, 1944), Mooney-Rivlin (Mooney, 1940; Rivlin & Rideal, 1948), Arruda-Boyce (Arruda & Boyce, 1993), Fung (Fung, 1981), and Ogden (Ogden & Hill, 1972) material models. There are also some further enhancements made possible by considerations of anisotropy (Gasser et al., 2006), viscoelasticity (Vogel et al., 2017), and poroelasticity (Selvadurai & Suvorov, 2017) that yield more physiologically realistic accounts of biological soft tissues. In addition to these, a model that couples electrical, thermal, and mechanical properties was introduced in 2005 (Erdem et al., 2005), but these will not be included in the scope of this work.

In the last decade, modeling of soft tissues has been a topic of interest to computational mechanicians. Behnke et al. introduced a thermo-viscoelastic model (Behnke et al., 2011) for a regular tubular geometry similar to the one used in our study. Petekkaya and Tönük (Petekkaya & Tönük, 2013) introduced an experimental study for in-situ determination of mechanical behavior of soft tissues. The study of Dogan and Celebi presented an experimental validation (Dogan & Celebi, 2016) and real time indentation response (Dogan & Serdar Celebi, 2010) of human liver that accounts viscoelastic characteristics in order to simulate surgery applications. Also, Gültekin et al. (Gültekin et al., 2019) introduced an alternative way to handle with the incompressibility in numerical applications. The aforementioned studies employed constitutive behaviors wherein derivation of an analytical solution to compare against poses considerable difficulty.

Analytical solutions to the mechanics of hyperelastic cylinders were examined in many aspects. Rivlin (Rivlin, 1948) investigated extension and torsion of circular cylindrical geometries made of neo-Hookean material, yet none of them was an inflation problem. Wineman (Wineman, 2005) formulated the problem of an inflating cylindrical tube by using the theory of elastic membranes which is valid only for thin-walled tubes. Zhu et al. (Zhu et al., 2010) examined short tubes under external pressure by the help of finite element method. Although they provided an analytical validation, the solution procedure wasn't presented therein. In 2011, an analytical solution for the extension, inflation and circumferential shearing of an annular cylinder was performed by Rajagopal and co-workers (Rajagopal & Saravanan, 2012). Their unconventional approach used strains as the dependent variables instead of stresses.

Breslavsky et al. (Breslavsky et al., 2016) presented an analytical solution to internally and externally pressurized circular rings made of neo-Hookean material to be used as a benchmark for checking the validity of finite element models. They have used shell theory. Their

formulation is based on the nonlinear shell assumption that defines the deformation at the midplane of the rings. On the other hand, the presented approach offers an analytical solution to the 1D axisymmetric continuum elastic formulation as a novel contribution to the existing literature. The purpose of obtaining an analytical solution is to serve as a benchmark for computational models. To demonstrate the outcome, a commercial finite element software, MARC (MSC Software, 2019) is used for validation.

2. THEORY OF ISOTROPIC HYPERELASTIC TUBES

Soft biological tissues are made up of matrix material, also known as the ground substance, which provides the grounds for the layout of other phases possibly made of fibers. This is so, for example, for the annulus fibrosus of the intervertebral discs or layers of arterial veins. The strain energy density, W combines various components in this composite material structure such as the matrix, the fibers, etc. In this section, we provide the continuum mechanics framework for formulating the boundary value problem posed by the internally pressurized thick cylinder (Cook & Young, 1999).

2.1. KINEMATICS OF TUBE INFLATION

Point coordinates in the initial (reference) configuration (R, Θ, Z) and in the deformed (current) configuration (r, θ, z) as shown in Figure 1. If the tube expands in an axially symmetric fashion, then $\theta = \Theta$ and furthermore deformed coordinates will not be a function of Θ so that $r = r(R, Z)$ and $z = z(R, Z)$. In addition, if the axial extension is applied uniformly and such that planes originally transverse to the longitudinal axis remains so after deformation, then the motion will not be a function of the axial position Z, either.
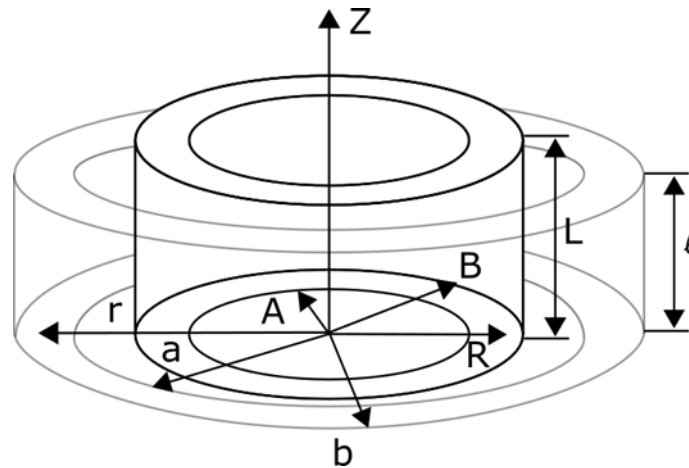

Figure 1:
Reference and Current Configurations of the Cylinder

We introduce $r = r(R)$ to represent the radial deformation function and the deformation mapping from the undeformed configuration to the deformed configuration becomes

$$r = r(R), \qquad \theta = \Theta, \qquad z = \lambda_l Z \tag{1}$$

where λ_l is the axial stretch which also known as the extension ratio. Stresses in an incompressible tube under inflation and uniform extension are considered. Radial deformation function can be written by the solution to differential equation of undeformed and deformed volumes as follows

$$r(R) = \left[a^2 + \lambda_l^{-1}(R^2 - A^2)\right]^{1/2} \tag{2}$$

The deformation gradient can be placed in matrix form as

$$F = \begin{bmatrix} r' & 0 & 0 \\ 0 & r/R & 0 \\ 0 & 0 & \lambda_l \end{bmatrix} \tag{3}$$

where r is the radial deformation function defined by Equation 2. Noting that the deformation gradient is in diagonal form, the terms in the diagonal become the principal stretches given as

$$\lambda_r = r', \lambda_\theta = r/R, \lambda_z = \lambda_l \tag{4}$$

Taking the polar decomposition $F = VR$ yields the rotation tensor $R = I$ and the left stretch tensor $V = C^{1/2}$. It is known that the incompressibility condition renders the hydrostatic part of the stress tensor as indeterminate. Thus, we introduce the term $-pI$. The scalar variable denoted by p is a Lagrange multiplier which does not contribute to the deformation but balances the large strains with the uniform tension or compression of the body. Replacing F with VR which leaves Cauchy stress tensor

$$\sigma = -pI + a_2 C + a_3 C^2 \tag{5}$$

where the coefficients $a_i, i = 2,3$ are

$$a_2 = \frac{2}{\sqrt{I_3}}\left(\frac{\partial W_0}{\partial I_1} + I_1 \frac{\partial W_0}{\partial I_2}\right), a_3 = \frac{-2}{\sqrt{I_3}}\frac{\partial W_0}{\partial I_2} \tag{6}$$

Expanding term by term, we arrive at the general form of the Cauchy stress components in terms of the principal stretch components

$$\begin{aligned} \sigma_{rr} &= -p + a_2\lambda_r^2 + a_3\lambda_r^4 \\ \sigma_{\theta\theta} &= -p + a_2\lambda_\theta^2 + a_3\lambda_\theta^4 \\ \sigma_{zz} &= -p + a_2\lambda_l^2 + a_3\lambda_l^4 \end{aligned} \tag{7}$$

If we take an isotropic material of neo-Hookean type behavior, the strain energy density function takes the form

$$W_0 = \frac{\mu}{2}(I_1 - 3) \tag{8}$$

Inserting this expression into Equation 6, the tensor coefficients are determined as $a_2 = \mu$ and $a_3 = 0$. Note that the incompressibility condition yields $I_3 = 1$. The final equations for the Cauchy stress components are evaluated by substituting in Equation 7 in terms of the deformation function r giving

$$\sigma_{rr} = -p + \mu(r')^2, \qquad \sigma_{\theta\theta} = -p + \mu\left(\frac{r}{R}\right)^2, \qquad \sigma_{zz} = -p + \mu\lambda_l^2 \tag{9}$$

Taking the deformation function r from Equation 2, it's derivative with respect to reference coordinate R yields

$$r' = \frac{\partial}{\partial R}\left[a^2 + \lambda_l^{-1}(R^2 - A^2)\right]^{1/2} = \frac{R/\lambda_l}{[a^2 + \lambda_l^{-1}(R^2 - A^2)]^{1/2}} = \frac{R}{r\lambda_l} \tag{10}$$

The equation of motion in Eulerian (current) description reads

$$\frac{\partial \sigma_{rr}}{\partial r} + \frac{1}{r}(\sigma_{rr} - \sigma_{\theta\theta}) = 0 \tag{11}$$

which gives upon substitution of σ_{rr} and $\sigma_{\theta\theta}$ from Equation 7

$$\frac{-\partial p}{\partial r} + \mu\frac{\partial(\lambda_r^2)}{\partial r} - \frac{\mu}{r}(\lambda_r^2 - \lambda_\theta^2) = 0 \tag{12}$$

Transforming the derivatives from r to R the above equation changes as

$$\frac{-\partial p}{\partial R} + 2\mu\lambda_r\frac{\partial \lambda_r}{\partial R} + \frac{\mu r'}{r}(\lambda_r^2 - \lambda_\theta^2) = 0 \tag{13}$$

Integrating the above expression from A to R, we solve for the intermediate hydrostatic pressure, $p(R)$ as

$$p(R) = c + \frac{\mu}{2\lambda_l}\left[log(\lambda_\theta^2\lambda_l) - \frac{a^2\lambda_l - A^2}{r^2\lambda_l}\right] \tag{14}$$

where c is an integration constant that remains to be determined. The model is subject to traction boundary conditions in the radial direction produced by the internal pressure, p_i and no external pressure. The pressure boundary condition on the inner boundary reads

$$\sigma_{rr}|_A = -p_i; \quad -p(A) + \frac{\mu A^2}{a^2\lambda_l} = -p_i \tag{15}$$

Evaluating the hydrostatic pressure term in Equation 14 at $R = A$ and inserting this into Equation 15, the integration constant can be solved as

$$c = p_i + \frac{\mu}{2\lambda_l}\left[1 + log\frac{A^2}{a^2\lambda_l} + \frac{A^2}{a^2\lambda_l}\right] \tag{16}$$

The two remaining unknowns that need to be solved for are a, the deformed internal radius and λ_l, the longitudinal stretch ratio. The solution depends on the axial mechanical condition. The model can either be set up under a condition of plane strain, or it can be left to contract freely in the longitudinal (z) direction, which is a generalized plane strain condition.

2.1.1. Plane Strain (PS) Condition

Under plane strain, the stretch ratio in the longitudinal direction becomes $\lambda_l^{ps} = 1$. In order to solve for a^{ps}, we evaluate the zero-pressure boundary condition at the outer surface of the tube which reads

$$\sigma_{rr|_B} = 0; \quad -p(B) + \frac{\mu\left(B/\lambda_l^{ps}\right)^2}{a^{ps2} + \lambda_l^{ps-1}(B^2 - A^2)} = 0 \tag{17}$$

This equation is non-linear in a. A numerical method can be employed for the determination of its roots. The plot given in Figure 2 indicates that the root of Equation 17 is between 11 and 12.

2.1.2. Generalized Plane Strain (GPS) Condition

In this case, λ_l^{gps} needs to be determined together with a^{gps}. For this, an extra equation is supplied from the mechanical equilibrium of the longitudinal sections in the z-direction. The line force f_z is simply the integral of normal longitudinal stress component (σ_{zz}) over the tube's thickness

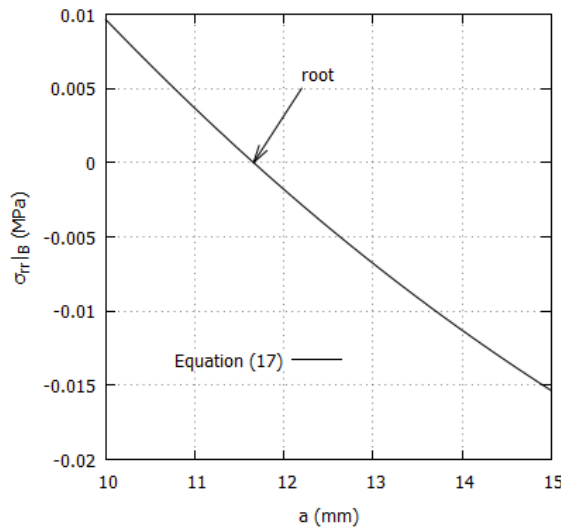$$f_z = \int_A^B \sigma_{zz}\, dr \tag{18}$$

Figure 2:
Plot of the Boundary Condition in Equation 17

Upon setting $f_z = 0$ and using this with the boundary condition (Equation 17), a system of two non-linear algebraic equations in a and λ_l are obtained. These can be solved by an appropriate numerical method. In our study, Maxima has been utilized as a symbolic mathematical manipulator for this purpose, and its results are presented in the Results section.

3. FINITE ELEMENT MODEL

Besides the analytical method's exact solution, the finite element method offers a faster way to deal with complicated problems within an acceptable level of accuracy. In the case of a simple geometry as in this study, it is possible to obtain the accuracy of the three-dimensional finite element implementation in MARC by comparing its solutions with the analytical solution. In this section, a series of finite element analysis is conducted by using MARC. The Neo-Hookean material model is used. Two different conditions were created in the longitudinal direction, the case of plane strain (PS), and that of generalized plane strain (GPS). Both the PS and GPS conditions are examined. A mesh sensitivity analysis is also presented for which a total of six consecutive refinements are used.

3.1. THE MESH

Throughout the sensitivity analysis, meshes are named as TyRx. The letter y indicates the number of elements in the Tangential direction and x is the number of elements in the Radial direction. A tube having 24 elements in the tangential direction, and one element in the radial and axial direction is created for the first mesh of the sensitivity analysis and called T24R1. This mesh is refined by halving the element size in the radial and tangential direction until reaching T768R32.
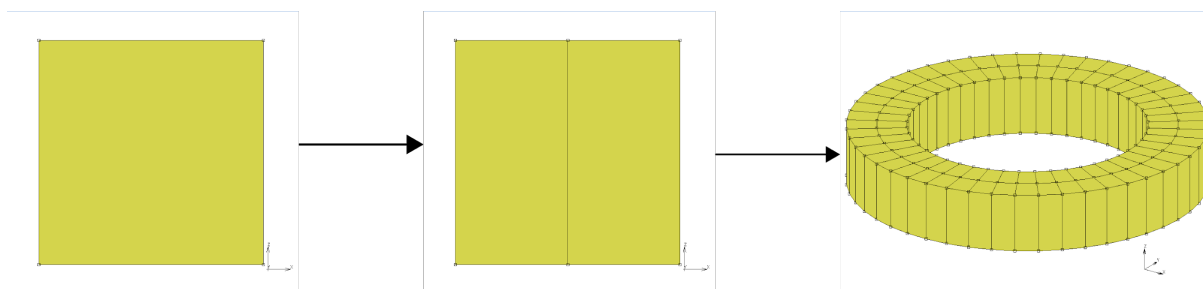

Figure 3:

Mesh Generation Steps: 1. Creation of a square shaped 2-D element (on the left). 2. Division into equal rectangles in radial direction (in the middle). 3. Revolving about axis of the cylinder (on the right).

A tube whose dimensions are 10 mm inner radius, 15 mm outer radius, and 5 mm height is considered. The mesh generation process is illustrated for the T768R32 mesh as follows. On the $X - Z$ plane, a square-shaped 2-D element is created whose nodes at Cartesian coordinates are (10,0,0), (15,0,0), (15,0,5) and (10,0,5). The finest mesh consists of 32 divisions in the radial direction biased towards the inner radius. These 32 elements are then revolved about the axis of symmetry to generate 768 layers in the circumferential direction. As a result, a total number of 24576 HEX8-type elements are created. Mesh generation steps are shown in Figure 3. For visual clarity, a mesh that has 2 elements in the radial direction and 48 elements in the tangential direction is given. Because the analysis scheme is built upon a cylindrical coordinate system, Cartesian nodal coordinates are transformed into cylindrical coordinates. This transformation is necessary to apply boundary conditions appropriately and retrieving the resulting field variables (stress, displacement, etc.) in polar cylindrical coordinates. Note that meshes in sensitivity analysis are generated in a similar manner.

In the case of large deformation incompressible analyses, Hermann elements (MARC element no.84) are used. Hermann element uses the mixed (u-p) formulation, which has an additional node to store hydrostatic pressure $p(R)$ at that location.

3.2. BOUNDARY CONDITIONS

Consideration of the nature of deformation induces a constraint which prevents all existing nodes from moving in the circumferential direction. This condition eliminates 24576 tangential degrees of freedom (DOF) in the finest mesh, thereby leading to significant reduction of the analysis time. The bottom face of the cylinder is prevented from moving in axial direction, which results in the elimination of 12288 more DOF. For the PS condition, the axial constraint is also applied at the top face of the cylinder which removes an additional 12288 equations. Under the GPS condition, all DOFs in the z-direction at the top face of the cylinder are tied to a single (master) node resulting in the elimination of 12286 equations.

3.3. LOADING

The cylinder is inflated with an inner pressure of 0.01 MPa in an incremental loading procedure consisting of 15 steps shown in Figure 4. The boundary conditions applied to the coarse mesh are shown in the inset of the same figure where load is illustrated with black arrows while red and blue arrows indicate displacement constraints along R and θ axes, respectively.
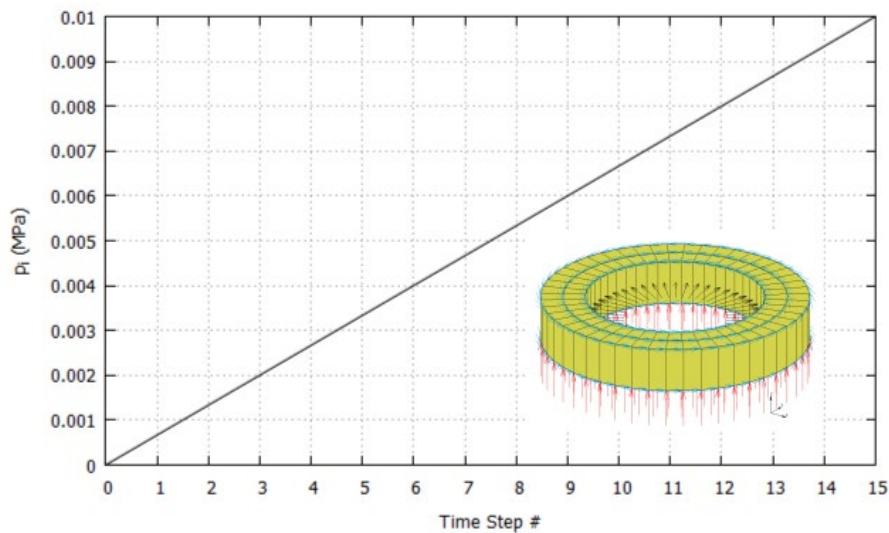

Figure 4:

Loading: Time step vs. inner pressure is given. The inner pressure p_i is applied in 15 equal increments. Besides, the loading is shown with black arrows in the subfigure. Red and blue arrows are the axial and the tangential displacement conditions, respectively.

It is known that the finite element method transforms distributed loads into nodal forces. Because the subject matter is a large deformation inflation process, under constant nodal forces the inner pressure decreases as a result of area enlargement, or vice versa. The Follower Force option, however, calculates distributed loads based upon the current configuration, taking into account the change in surface area, and maintaining a constant inner pressure throughout the analysis. Overall, in MARC, Large Strain and Follower Force options are turned ON.

3.4. MATERIAL

While fully incompressible deformation can be satisfied by setting $det(C) = 1$ in continuum mechanics, it is not so for the nearly incompressible formulation in MARC's Hermann element. This HEX8 type three-dimensional finite element utilizes (u-p) formulation

where an extra degree-of-freedom is used to store the element-wise hydrostatic pressure alleviating locking behavior associated with the displacement formulation elements. Nearly incompressible behavior is achieved by increasing the Poisson's ratio to get as close to 0.5 as possible. In MARC, this is done indirectly by assigning the bulk modulus to take very large values. "Assumed Strain" and "Constant Dilatation" options are activated for the geometric property assignment. Assumed Strain formulation is generally used to capture linear variation in shear strain in bending. Nevertheless, this option is set to ON in our problem. Updated Lagrangian Formulation is selected as the solution procedure.

The strain energy density function of a neo-Hookean material is given in Equation 8. However, MARC's formulation is slightly different. In MARC, hyperelastic materials are denoted as elastomers. MOONEY model definition is used to activate such a material option. MOONEY definition consists of five elasticity constants. The neo-Hookean behavior can be achieved by setting all these constants to zero except C_{10}. Then strain energy density function reduces to:

$$W = C_{10}(I_1 - 3) \tag{19}$$

Noting the difference between Equation 8 and Equation 19, the elasticity parameter is set to half of the initial shear modulus: $C_{10} = 0.035$ MPa. Nearly incompressible behavior is satisfied automatically by assigning the bulk modulus to be 10^4 times C_{10}.

4. RESULTS & DISCUSSION

The solutions for the PS and GPS cases are provided for a cylinder geometry which has an inner radius $A = 10$ mm, and an outer radius $B = 15$ mm before deformation, a shear modulus of a neo-Hookean model $\mu = 0.070$ MPa, and subjected to an internal pressure $p_i = 0.01$ MPa. The results of the neo-Hookean model, which happens to be widely used to represent ground substance in soft tissues, can be used to pinpoint discrepancies in commercial softwares such as MARC as pointed out in section 4.6.

The solution for the PS condition can be found by solving the boundary condition in Equation 17 for $R = B$ and $\lambda_l = 1$ yields

$$a = 11.6609 \tag{20}$$

For the GPS condition unknown λ_l is to be solved in addition to a. A system of two non-linear equations which comprised by the boundary conditions Equations 17 and 18, are solved yielding the unknowns

$$a = 11.8283, \qquad \lambda_l = 0.956344 \tag{21}$$

4.1. MESH SENSITIVITY ANALYSIS

Cauchy stress at points lying along the radial direction are given in Figure 5 for different mesh sizes. The stress values at intermediate locations on the R-axis converged faster than those at the inner and outer radii. The results are seen to be most sensitive to the mesh size at the inner wall of the tube where the pressure is applied. So, the final T768R32 mesh is biased towards the center of the tube to increase the accuracy of stresses in this region.
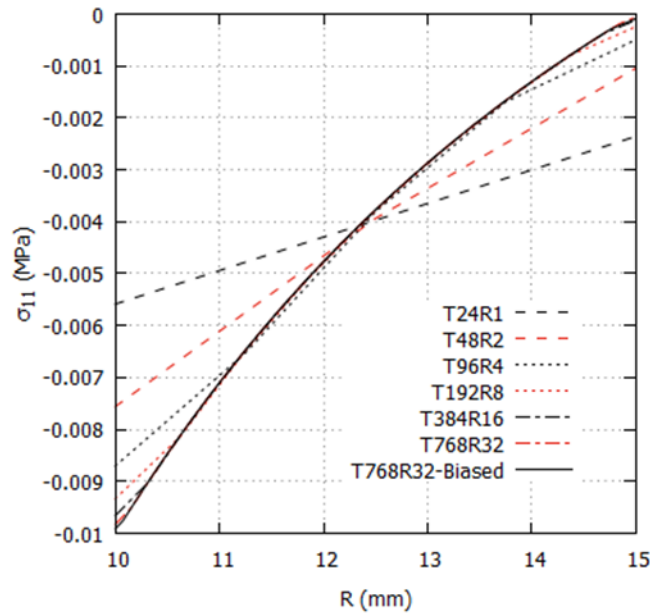
Figure 5:

Radial Stress Along R for Different Mesh Sizes: The solid line is the finest mesh which has a finer mesh density near the inner wall rather than the outer wall. The first and the second numbers in TxxRyy code depict the number of elements in tangential and radial directions.
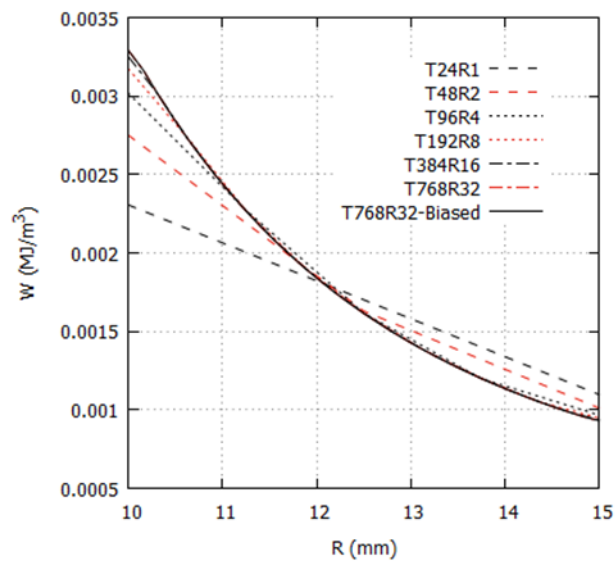

Figure 6:

Strain Energy Density Along R for Different Mesh Sizes: The solid line is the finest mesh which has a finer mesh density near the inner wall rather than the outer wall. The first and the second numbers in TxxRyy code depict the number of elements in tangential and radial directions.

Total strain energy density also changes as a function of position along the radial direction as plotted in Figure 6. The inner wall retains its importance in terms of mesh sensitivity of strain energy density results. However, it is seen that the rate of convergence of total strain energy density is much faster than the radial Cauchy stress component.
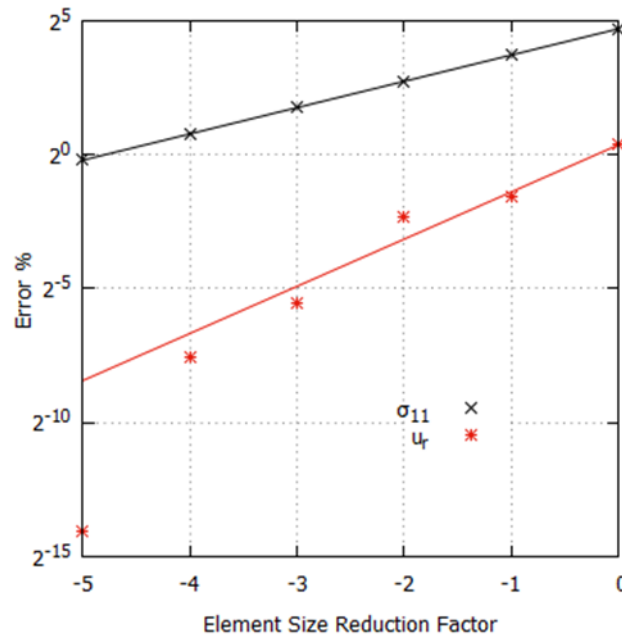
Figure 7:

The Displacement and the Stress Error with Respect to Analytical Solution: Radial stress (σ_{rr}) and displacement (u_r) are given as black and red, respectively. X-axis value represents the exponential factor used in controlling the element size.

As for the mesh verification, convergence rates of displacement and stress results are obtained for a point that lies on the inner surface of the tube ($R = A$) as shown in Figure 7. In agreement with observations from the two previous figures, the convergence rate of stress is $O(h)$ which is an order less than that of the displacement $O(h^2)$. It is also striking that, while the error in u_r is just above 1% for the coarsest mesh (T24R1), the error in σ_{11} falls barely under 1% for the finest (Biased T768R32). This difference is quite expected as calculation of stress in finite elements depends on the derivative of displacements, which induces a huge loss of accuracy in the derived quantities.

Following verification, validation against the analytical solutions of the PS and GPS cases are illustrated in the following sections. Based on the results of the verification step above, validation is performed using the densest T768R32 mesh with radial biasing applied towards the inner surface.

4.2. NUMERICAL STABILITY

The solution of the PS condition converged in 15 cycles (iterations) while the GPS did in 45 cycles (3 cycles per load increment). The extra iterations for the GPS condition were necessary to achieve force equilibrium at the top face of the tube where nodal longitudinal DOFs are linked. An equal number of cycles per increment throughout the analysis for both conditions was accepted as a positive indicator of numerical stability.
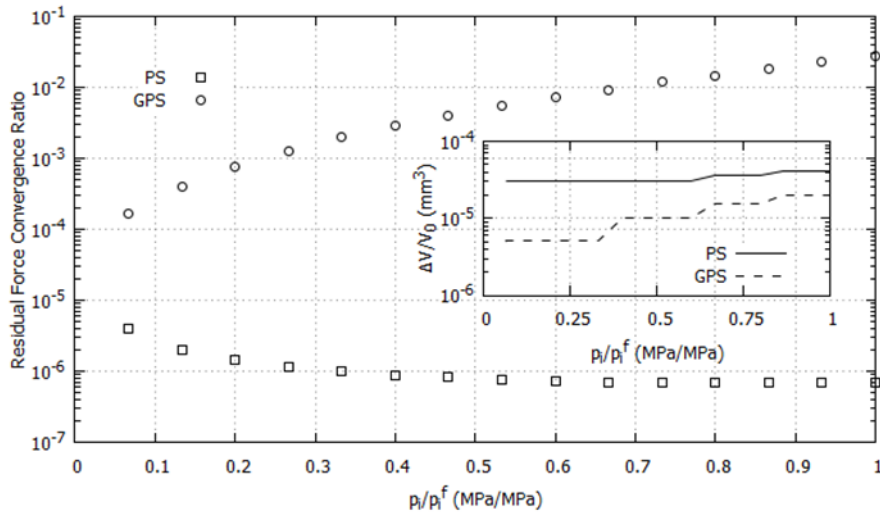
Figure 8:

Residual Force Convergence Ratio and Volume Change Ratio vs. Loading Factor: On abscissa, inner pressure p_i increases up to final pressure value p_i^f. Residual force convergence ratio is on ordinate which scaled logarithmically. PS and GPS conditions are given as squares and circles, respectively. In subplot, the volume change ratio is given against the loading factor. PS condition is given as solid line. GPS condition is given as dashed line.

The convergence criterion is based on the Residual Convergence Ratio (RCR) in MARC, which is the ratio of maximum residual force over the maximum reaction force. The default convergence tolerance for RCR was 0.1. The evolution of the RCR with increasing load is depicted in Figure 8 for the PS as well as the GPS conditions. The large difference between the RCR data is attributed to the difference in the longitudinal reaction force between the two conditions. A high reaction force develops in the longitudinal direction under the PS condition, which results in a quick drop in the RCR as loading proceeds. However, the reaction force is much lower for the GPS case, which results in a much higher RCR, approaching the convergence tolerance towards the end of the loading.

As MARC provided no support for full incompressibility in any of its elements, the level of compressibility was monitored using the difference between the current and original volumes. The ratio of the volume difference to the current volume is shown as an inset in Figure 8 for increasing loads. Although this ratio remained below 10^{-4} for both cases, the GPS condition behaved more nearly incompressible in comparison to the PS case.

4.3. DEFORMATION OF THE TUBE

The tube deforms in the radial direction as depicted in Figure 1. There is no displacement in the circumferential direction ($u_\theta = 0$) due to the axisymmetric nature of the problem. As a result of positive internal pressure, the radial displacements are all positive, indicating a radial expansion of the tube. In the axial (longitudinal) direction, no displacements are allowed by the PS condition, while the tube shortens under the GPS condition.
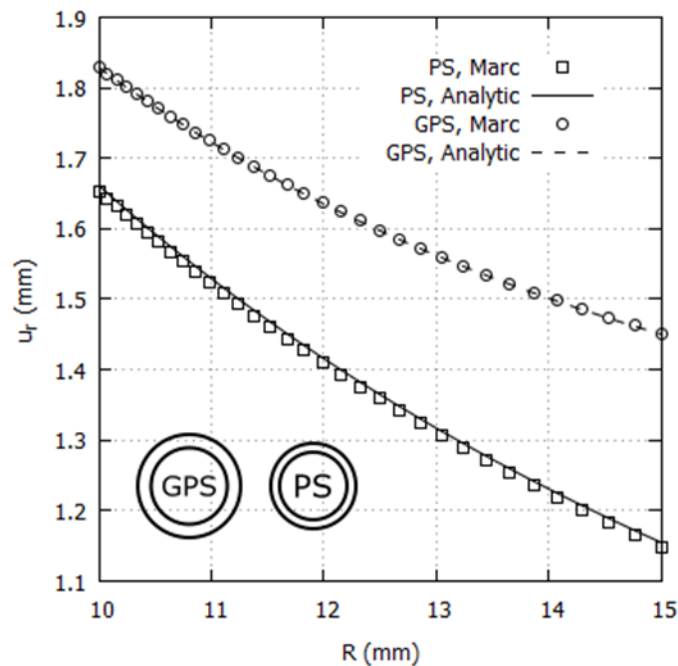
Figure 9:
Radial Displacement Along R: The radial displacement is plotted through the wall thickness of the cylinder. Squares and solid line are used for PS. Circles and dashed line are used for GPS. Final configuration of cylinders in both cases are given the left bottom corner.

Radial displacement plotted along the radial line decreases from the inner surface monotonically towards the outer as shown in Figure 9. No axial displacement occurs in the PS condition, while an axial displacement $u_z = 0.2190$ mm occurs in GPS. This is accurate to within one-hundredth of a percent compared with the value calculated using the longitudinal stretch from the analytical solution. Radial displacement data obtained from finite element analysis fits perfectly on the analytical solution when the GPS condition is the subject of interest. On the PS side, however, MARC's values are slightly lower than the analytical line, but this is still well accurate. Because the GPS condition is a slightly less constrained configuration than the PS, it displaces more. A larger difference between the inner and outer displacements for the case of PS condition indicates that its wall thickness gets thinner than that of the GPS condition as a result of inflation as shown in the inset of Figure 9.

4.4. STRESSES IN THE TUBE

Radial Cauchy stress (σ_{11}) results agree with the applied boundary conditions at the inner and outer surfaces (Figure 10). The PS and GPS cases yield identical radial stress profiles which are in agreement with the thick-walled cylinder solution of elasticity (Cook & Young, 1999). Finite element results are lying atop of analytical curves. It was shown in Figure 5 for different meshes that the geometrical boundaries (inner and outer walls) were most sensitive to mesh sizes.

The plot of circumferential stress (σ_{22}) along a radial line from the inner to the outer surface is given in Figure 11. Although the stresses under the PS condition are slightly higher than the GPS case, there is virtually no difference between them. The finite element results fall slightly below the analytical curves under both conditions but there is a remarkable fit between the numerical and computational solutions. For the given model geometry, the ratio of

maximum circumferential stress to the applied pressure remains between 3.3 and 3.4, which
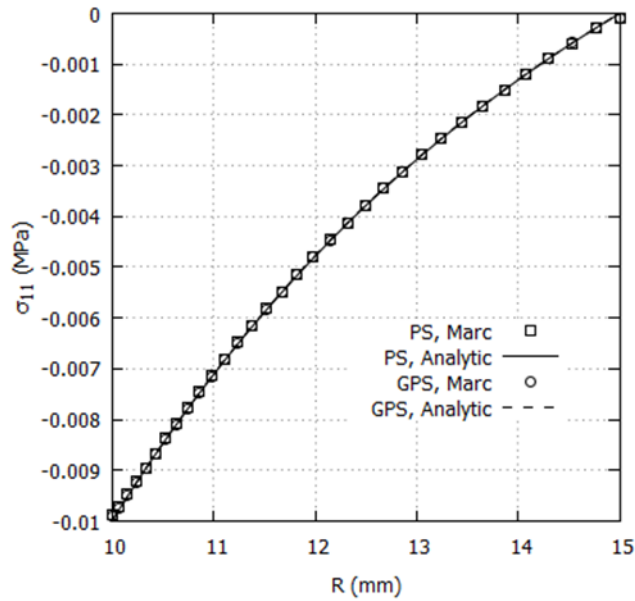
agrees well with (Cook & Young, 1999).

Figure 10:
Radial Stress Along R: The radial stress is plotted through the wall thickness of the cylinder. Squares and solid line are used for PS. Circles and dashed line are used for GPS.
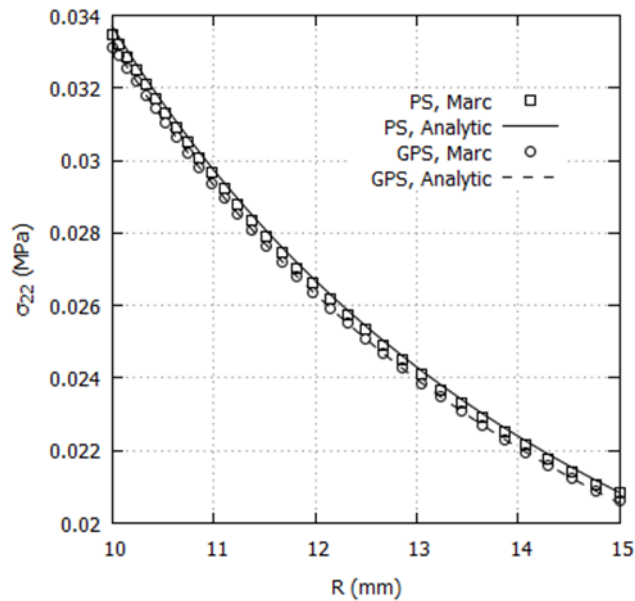

Figure 11:
Circumferential Stress Along R: The circumferential stress is plotted through the wall thickness of the cylinder. Squares and solid line are used for PS. Circles and dashed line are used for GPS.

Figure 12 represents the radial variation of axial stress (σ_{33}) from the inner to the outer surface. Axial stress is much higher under PS condition as expected due to the constraint preventing longitudinal shortening of the body. This results in axial tensile stresses with the same order of magnitude as the internal pressure. The axial stresses under GPS condition,

however, remain below 10% of the applied internal pressure. The self-equilibrating nature of reaction forces at the top surface of the tube results in a state of stress that is compressive in the inner part of the tube and tensile in the outer part. The axial stresses become neutral between these two regions roughly in the middle of the wall.
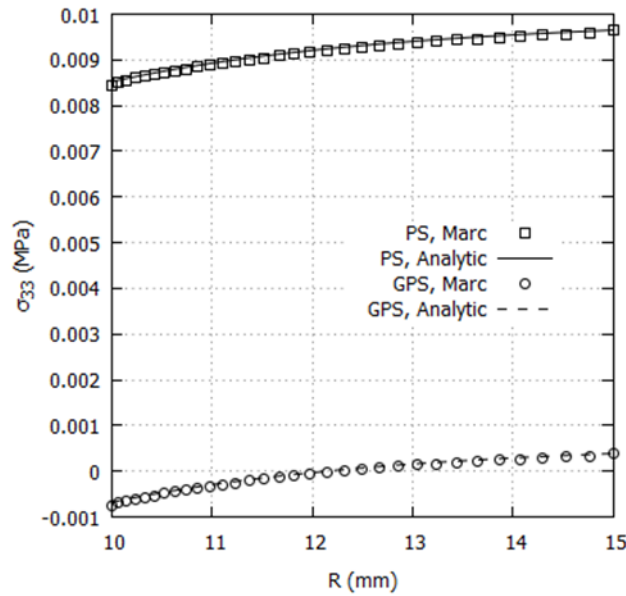

Figure 12:
Axial Stress Along R: The axial stress is plotted through the wall thickness of the cylinder. Squares and solid line are used for PS. Circles and dashed line are used for GPS.

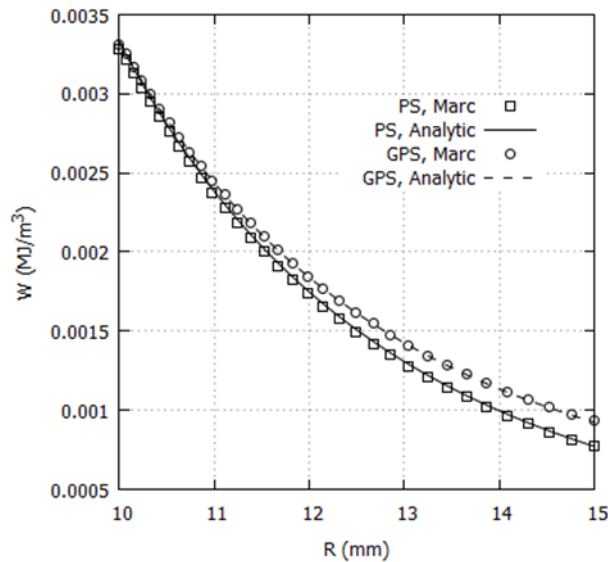## 4.5. STRAIN ENERGY AND HYDROSTATIC PRESSURE IN THE TUBE

Figure 13:
Strain Energy Density Along R: The circumferential stress is plotted through the wall thickness of the cylinder. Squares and solid line are used for PS. Circles and dashed line are used for GPS.

Looking at the stored strain energy per material volume (Figure 13), the cylinder in the case of GPS experiences larger strains than those in the case of PS, especially at the outer wall of the cylinder. On the inner wall, they are almost the same. The finite element solution agrees with the analytical solution for both cases.

Figure 14 indicates the hydrostatic pressure as a function of R. The hydrostatic pressure under the PS and GPS conditions are both more than 6 times the internal pressure. The reason for such high pressure is attributed to the application of incompressibility constraint. Interestingly, the hydrostatic pressure under the GPS condition is slightly higher than the PS, despite the over-constrained nature of PS.
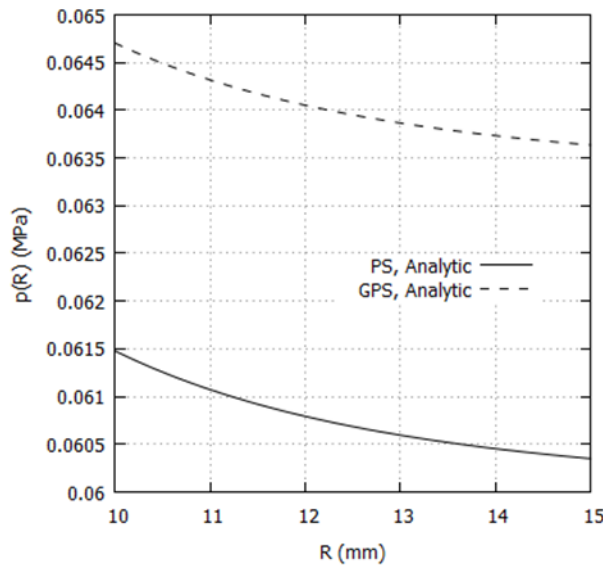

Figure 14:
Hydrostatic Pressure Along R: PS and GPS conditions are given as solid and dashed lines, respectively.

4.6 STRAINS IN THE TUBE

While representing finite strains it is benefited from two different definitions. Lagrange and Almansi circumferential strain magnitudes are calculated analytically via Equation 22 and 23, respectively.

$$E_{\theta\theta} = \frac{1}{2}(\lambda_\theta^2 - 1) \tag{22}$$

$$e_{\theta\theta} = \frac{1}{2}\frac{\lambda_\theta^2 - 1}{\lambda_\theta^2} \tag{23}$$

Applying these to our problem and plotting with numerical result obtained with MARC gives graphs in Figure 15. The first observation is that the tangential strains in GPS condition are larger than of PS condition through entire radius of the tube. Strains decay exponentially from inner wall to outer wall of the hollow cylinder. The difference between Lagrangian and Eulerian approach can be easily seen in both graphs. It is critical to note that the MARC's only available strain output agrees with neither of them but follows the arithmetic average of the circumferential strain magnitudes given in above equations. Here, the significance of verification comes in view. Not only self-developed finite element codes but also enhanced

commercial tools should have a benchmark solution and one should not trust blindly in a
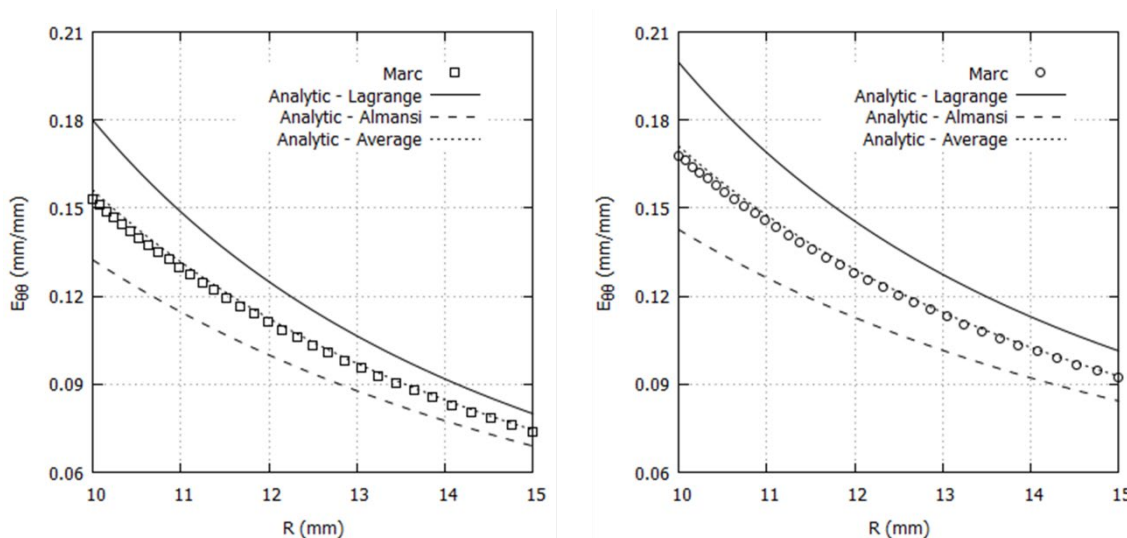
commercial software.

Figure 15:
Circumferential Strain Along R: The circumferential strain is plotted through the wall thickness of the cylinder. PS case is on the left. GPS case is on the right. Squares and circles are discrete solution of finite element for respective cases. Lagrange, Almansi and average strain solutions are plotted with solid, dashed and dotted lines, respectively.

5. CONCLUSION

Today, finite element software comprises the most popular and useful tool in dealing with complicated problems from solid mechanics, in both industrial product development as well as academic research. However, it is usually forgotten that their formulations are based on a theoretical framework called continuum mechanics. Although developments in continuum mechanics lost its momentum with the increasing availability of computing power, analytical solutions are still very useful to validate numerical tools such as finite elements. In this context, the inflation mechanics of a tube composed of a neo-Hookean material was studied by using both analytical as well as the finite element method.

Plane strain and generalized plane strain solutions of tube inflation have been derived using continuum mechanics. Also, a commercial finite element software was employed to obtain numerical results. The numerical results were shown to be self-consistent and hence were verified. In addition, the differences between plane strain and generalized plane strain solutions were highlighted. As a result of the benchmark study, we observed that the finite element method yielded highly accurate results with appropriate mesh refinement, however, it was also observed that the non-linear strain output from MARC 2019.0.0 did not match with the analytical solution attributed to a bug in the commercial software.

The solution also provided an understanding of the inflation mechanics of a tubular structure made of soft tissue. Under plane strain condition the tube experienced higher stresses in all principal directions except the radial. On the contrary, when placed under generalized plane strain condition, the tube experienced higher displacements and strains. So, it stored more energy within its volume under the GPS condition. Moreover, an unexpected level of hydrostatic pressure was recorded under both the PS and GPS conditions, which was higher than 6 times the applied internal pressure.

Although fiber embedded models were not considered in this paper, their contribution to the mechanics of biological tissue cannot be neglected. The derivation of an analytical solution based on continuum mechanics for the fiber-embedded hyperelastic tissue however is left as a future study.

ACKNOWLEDGEMENTS

We would like to thank Mr. Cevat Volkan Karadağ (M.Sc., ME) for reading through the entire manuscript and providing valuable comments and corrections.

CONFLICT OF INTEREST

Author(s) approve that to the best of their knowledge, there is not any conflict of interest or common interest with an institution/organization or a person that may affect the review process of the paper.

AUTHOR CONTRIBUTION

Ömer Faruk Büyükkaya obtained computational data and the analytical model while he was pursuing his graduation project in the undergraduate mechanical engineering program. Ali Fethi Okyar supervised this project and contributed in the writing.

REFERENCES

1. Arruda, E. M., & Boyce, M. C. (1993). A three-dimensional constitutive model for the large stretch behavior of rubber elastic materials. *Journal of the Mechanics and Physics of Solids*, *41*(2), 389–412. https://doi.org/10.1016/0022-5096(93)90013-6

2. Behnke, R., Dal, H., & Kaliske, M. (2011). An extended tube model for thermo-viscoelasticity of rubberlike materials: Parameter identification and examples. *PAMM*, *11*, 353–354. https://doi.org/10.1002/pamm.201110168

3. Breslavsky, I. D., Amabili, M., Legrand, M., & Alijani, F. (2016). Axisymmetric deformations of circular rings made of linear and Neo-Hookean materials under internal and external pressure: A benchmark for finite element codes. *International Journal of Non-Linear Mechanics*, *84*, 39–45. https://doi.org/10.1016/j.ijnonlinmec.2016.04.011

4. Cook, R. D., & Young, W. C. (1999). Pressurized cylinders and spinning disks. In *Advanced Mechanics of Materials*. Prentice Hall.

5. Dogan, F., & Celebi, M. S. (2016). Quasi-non-linear deformation modeling of a human liver based on artificial and experimental data. *The International Journal of Medical Robotics and Computer Assisted Surgery*, *12*(3), 410–420. https://doi.org/https://doi.org/10.1002/rcs.1704

6. Dogan, F., & Serdar Celebi, M. (2010). Real-time deformation simulation of non-linear viscoelastic soft tissues. *Simulation*, *87*(3), 179–187. https://doi.org/10.1177/0037549710364532

7. Erdem, A., Usal, M., & Usal, M. (2005). Keyfi fiber takviyeli viskoelastik piezoelektrik bir cismin elektro-termomekanik davranışı için matematiksel bir model. *Gazi Üniversitesi Mühendislik Mimarlık Fakültesi Dergisi*, *20*(3), 305–319.

8. Fung, Y. C. (1981). Bio-viscoelastic solids. In *Biomechanics: Mechanical Properties of Living Tissues* (2nd ed., pp. 196–260). New York, NY: Springer New York. https://doi.org/10.1007/978-1-4757-1752-5_7

9. Gasser, T. C., Ogden, R. W., & Holzapfel, G. A. (2006). Hyperelastic modelling of arterial layers with distributed collagen fibre orientations. *Journal of the Royal Society, Interface*, *3*(6), 15–35. https://doi.org/10.1098/rsif.2005.0073

10. Goodno, B. J., & Gere, J. M. (2016). Applications of plane stress: pressure vessels. In *Mechanics of Materials* (9th ed.). Cengage Learning.

11. Gültekin, O., Dal, H., & Holzapfel, G. A. (2019). On the quasi-incompressible finite element analysis of anisotropic hyperelastic materials. *Computational Mechanics*, *63*(3), 443–453. https://doi.org/10.1007/s00466-018-1602-9

12. Mooney, M. (1940). A theory of large elastic deformation. *Journal of Applied Physics*, *11*(9), 582–592. https://doi.org/10.1063/1.1712836

13. MSC Software. (2019). MARC/Mentat 2019.0.0. Irvine, CA, USA.

14. Ogden, R. W., & Hill, R. (1972). Large deformation isotropic elasticity-on the correlation of theory and experiment for incompressible rubberlike solids. *Proceedings of the Royal Society of London. A. Mathematical and Physical Sciences*, *326*(1567), 565–584. https://doi.org/10.1098/rspa.1972.0026

15. Petekkaya, A., & Tönük, E. (2013). Yumuşak biyolojik dokuların düzlemsel eşyönsüz mekanik davranışının bireye ve noktaya özel belirlenmesi için elipsoid uçlarla yerinde canli (in vivo) indentör deneyleri. *Gazi Üniversitesi Mühendislik Mimarlık Fakültesi Dergisi*, *26*(1), 63–72.

16. Rajagopal, K. R., & Saravanan, U. (2012). Extension, inflation and circumferential shearing of an annular cylinder for a class of compressible elastic bodies. *Mathematics and Mechanics of Solids*, *17*(5), 473–499. https://doi.org/10.1177/1081286511423125

17. Rivlin, R. S. (1948). Large elastic deformations of isotropic materials. III. Some simple problems in cyclindrical polar co-ordinates. *Philosophical Transactions of the Royal Society of London. Series A, Mathematical and Physical Sciences*, *240*(823), 509–525. https://doi.org/10.1098/rsta.1948.0004

18. Rivlin, R. S., & Rideal, E. K. (1948). Large elastic deformations of isotropic materials IV. further developments of the general theory. *Philosophical Transactions of the Royal Society of London. Series A, Mathematical and Physical Sciences*, *241*(835), 379–397. https://doi.org/10.1098/rsta.1948.0024

19. Selvadurai, A. P. S., & Suvorov, A. P. (2017). On the inflation of poro-hyperelastic annuli. *Journal of the Mechanics and Physics of Solids*, *107*, 229–252. https://doi.org/https://doi.org/10.1016/j.jmps.2017.06.007

20. Treloar, L. R. G. (1944). Stress-strain data for vulcanised rubber under various types of deformation. *Trans. Faraday Soc.*, *40*(0), 59–70. https://doi.org/10.1039/TF9444000059

21. Vogel, A., Rakotomanana, L., & Pioletti, D. P. (2017). Chapter 3 - viscohyperelastic strain energy function. In Y. Payan & J. Ohayon (Eds.), *Biomechanics of Living Organs* (Vol. 1, pp. 59–78). Oxford: Academic Press. https://doi.org/https://doi.org/10.1016/B978-0-12-804009-6.00003-1

22. Wineman, A. (2005). Some results for generalized neo-Hookean elastic materials. *International Journal of Non-Linear Mechanics*, *40*(2–3), 271–279. https://doi.org/10.1016/j.ijnonlinmec.2004.05.007

23. Zhu, Y., Luo, X., Ogden, R., Zhu, Y., Luo, X., & Ogden, R. (2010). Nonlinear axisymmetric deformations of an elastic tube under external pressure. *European Journal of Mechanics-A/Solids*, *29*(2), 216–229. https://doi.org/10.1016/j.euromechsol.2009.10.004ï